Advanced Robotics

ISSN: 0169-1864 (Print) 1568-5535 (Online) Journal homepage: http://www.tandfonline.com/loi/tadr20

A novel tri-axial capacitive-type skin sensor

Sophon Somlor, Richard Sahala Hartanto, Alexander Schmitz & Shigeki Sugano

To cite this article: Sophon Somlor, Richard Sahala Hartanto, Alexander Schmitz & Shigeki Sugano (2015) A novel tri-axial capacitive-type skin sensor, Advanced Robotics, 29:21, 1375-1391, DOI: 10.1080/01691864.2015.1092394

To link to this article: http://dx.doi.org/10.1080/01691864.2015.1092394

Published online: 05 Nov 2015.

Advanced Robotics, 2015
Vol. 29, No. 21, 1375–1391, http://dx.doi.org/10.1080/01691864.2015.1092394

FULL PAPER

A novel tri-axial capacitive-type skin sensor

Sophon Somlor[a]*, Richard Sahala Hartanto[a], Alexander Schmitz[a] and Shigeki Sugano[b]

[a]*Sugano Laboratory, School of Creative Science and Engineering, Waseda University, Okubo 2-4-12, Shinjuku, Tokyo 169-0072, Japan;* [b]*Department of Modern Mechanical Engineering, School of Creative Science and Engineering, Waseda University, Ookubo 3-4-1, Shinjuku, Tokyo 169-8555, Japan*

(*Received 19 January 2015; revised 6 June 2015; accepted 6 August 2015*)

This paper introduces a novel tri-axial capacitive force sensor. The sensor can measure the force vector, is embedded in soft 7 mm-thick silicone skin, enables temperature sensitivity compensation and has digital output. To measure the force vector, tilted capacitive sensor elements are used which are facing in different directions to differentiate the tangential forces. The sensor is intended for distributed contact sensing in a robotic skin, but could be also used for other applications such as novel haptic user interfaces in wearable devices. A series of experiments was performed and showed good sensor characteristics. The concept of the tilted force transducers has been proven to have the capability of detecting the force vector acting on the local sensor surface.

Keywords: tri-axial force; capacitance measurement; humanoid robot; tactile sensing; force sensing

1. Introduction

The sense of touch is an important ability not only for humans, but also for robots.[1] Due their location, distributed tactile sensors in the skin provide the most direct feedback of the interaction with the environment, and measuring the contact forces is crucial to ensure a safe and robust interaction of a robot with unknown environments. Furthermore, tactile sensors provide important information for manipulation, exploration and haptics.[2] Touch sensors can be used, for example, for in-hand manipulation [3] or to identify objects even without visual information.[4]

Distributed touch sensing for robotic skins has many requirements. First, the transducers have to fit into a thin robotic skin. In humanoid robots, the available space is limited. Besides the space for the transducers, the space for the readout circuit and the wires for a high number of distributed sensor elements need to be taken into account. Furthermore, ideally the skin should be soft, in order to guarantee safe interaction of the robot with its surrounding, especially humans, and to assist in object manipulation. In order to achieve soft skin, compliant material (usually viscoelastic material such as silicone) needs to be integrated into the skin.[5,6] Placing the compliant layer above the sensors leads to a reduction of the sensitivity, spatial resolution and time response of the sensor.[7] If the compliant material is part of the transducer as in [8], this usually leads to severe hysteresis in the sensor measurements. Therefore, ideally the compliant material is placed below the transducers and the transducers are placed as close as possible to the skin surface, which is beneficial, for example, for the sensitivity and a faster time response. However, in several sensors, the transducer is more rigid than the compliant material. Putting this rigid transducer directly at the outermost surface could lead to injury in human–robot interaction. Therefore, some recent works have put efforts in solving the problem of reduced sensitivity when a layer of compliant material is placed on top of a sensor. Incorporating a layer of air into the sensor instead of bulk silicone increases the sensitivity and can mitigate the problem of hysteresis to some extent.[9] A combination of hard columnar and soft conical force transducers made of silicone can minimize the sensitivity reduction of the thick compliant layer as well.[10]

Many sensors are too big to be integrated into thin skin. For the sensors that have been integrated into thin skin, one major limitation is that most of them measure only normal forces, not tangential forces.[5,11] Tangential forces are an important component of the interaction forces, and information about the tri-axial contact forces would make object manipulation and recognition tasks easier. For example, the weight of a grasped glass that is filled with water, the force that is being applied while using a hammer or possibly the surface curvature of a grasped object could be evaluated. Measuring distributed force vectors directly at the impact sites could also lead to improved collision reaction and impedance control possibilities.

In this paper, a novel design with tilted capacitive sensors is proposed, as shown in Figure 1. The sensor elements are facing in different directions and as a result the tangential forces can be differentiated. Furthermore, this design has the benefit that the transducers can bend;

*Corresponding author. Email: sophon@sugano.mech.waseda.ac.jp

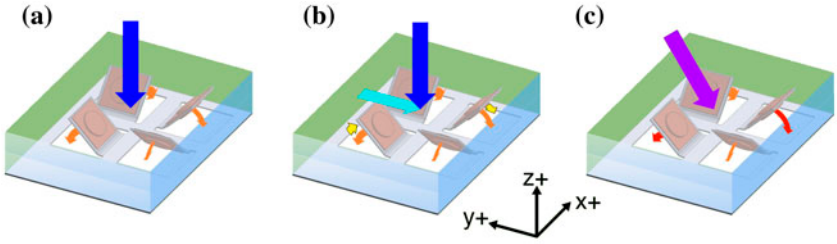

Figure 1. The shear force detection principle of the proposed skin sensor. (a) When a normal load (blue) is applied to the top of the sensor, all four sensing units sense the force (orange). (b) When a shear force (cyan) is added, the force sensed by the pair of two perpendicular sensing units becomes increased and decreased, respectively (yellow). (c) The resultant forces of input force (purple) and the sensed forces of all four units (red and orange) are shown.

therefore, compliant material can be placed below them. Accordingly, without reducing the compliance, the transducers can be placed closer to the skin surface, which is beneficial as discussed above. Finally, the tilted arrangement allows more sensors to fit in the same space, which could lead to a higher spatial resolution.

During the implementation, the other requirements of distributed touch sensors were also taken into consideration. In particular, the sensors are embedded in soft silicone, to guarantee a soft exterior. Moreover, an AD7147 capacitance-to-digital converter (CDC) chip is used to digitize the sensors locally, as in [8]. A temperature sensing pad is included, to compensate the influence of temperature changes on the measurements, as in [5]. For the transducer, a copper beryllium plate is used, as described in [11], but with an improved shape to foster a parallel deformation, in order to achieve a higher sensitivity and range.[12] Copper beryllium has excellent spring properties. Nevertheless, as the transducers are embedded in soft silicone, hysteresis in the sensor measurements can be expected, which will be experimentally evaluated. As a flexible printed circuit board (PCB) is used, the sensor can be applied on curved surfaces, even though the copper beryllium plates and the integrated chip somewhat limit the flexibility.

The remainder of this paper is structured as follows. In the next section, related work is presented. Section 3 describes the sensor concept and how the sensor is implemented. Section 4 presents the experiments that have been performed to evaluate the sensor performance. The sensor responses before and after the molding of the skin are compared. The force vector detection of the molded sensor is evaluated. Finally, in Section 5, the results of the experiments are discussed and the conclusion and future work are presented.

2. Related work

There are many sensing principles which can be employed for tactile sensing.[1] We will focus our discussion on sensors that are capable of measuring shear forces and related capacitive sensors. For a more in-depth discussion of different transduction technologies and integration issues in robotic systems, please refer to the recent review papers.[2,13,14]

Piezoelectric sensors can detect changes in force; a single piezoelectric sensor embedded in a soft substrate can detect changes in normal as well as in shear forces, but cannot distinguish them. Piezoelectric sensors based on PVDF have been incorporated into several robotic hands,[15–17] and can be used, for example, to detect slippage. Hosoda et al. [18] built an anthropomorphic robotic fingertip with randomly distributed strain gauges and PVDF films embedded in silicone rubber. Experiments were carried out for discriminating several materials through pushing and rubbing. The CB2 humanoid robot's body [19] is covered all over with 197 sensors based on PVDF films. In [17,18], the piezoelectric sensors were embedded in soft skin, but in none of the aforementioned implementations the force vector (the direction of applied force) can be measured. Touchence[1] sells a thin, small-sized 3-axis tactile sensor based on MEMS piezoelectric elements, but the sensor is rigid and the necessary electronics are bigger than the sensor itself.

Many optical sensors that can measure shear forces are too big to be integrated into skin that is only several millimeters thick, as they need a camera to look at the skin, for example, in [20,21]. A small-sized optical sensor that can measure both normal and shear forces was already proposed more than 10 years ago in [22], but to the best of the authors' knowledge, it has not been integrated in a robotic system yet. Optical 3-axis sensors have also been integrated into soft sensor flesh,[23] and those sensors have recently been made commercially available by Touchence. The highly sensitive 3-axis distributed sensors in [10] were designed for robotic fingertips with a height of 42.6 mm and width of 27 mm. A 10 mm wide and 8 mm high optical sensor that can measure the force vector is currently available from OptoForce.[2]

The Obrero hand [24] has 40 dome-like sensors made from silicone rubber. The position of a magnet in the tip of each dome is sensed by four Hall Effect sensors located in the base of the dome, and therefore allows shear force measurement. A 1-axis soft Hall Effect tactile sensor for robotic fingertips and phalanges was recently proposed in [9]; the sensor has a smooth surface and provides high sensitivity because it incorporates an extra layer of air to increase the deformability. In [25], a sensor based on pressure-sensitive conductive rubber is described, which also uses a dome-like structure above the sensors. In general, a dome-like structure can assist in sensing the shear forces; however, a smooth skin surface is preferable in many applications.

A lot of sensors that can measure 3-axis or even 6-axis F/T are based on strain gauges, but many are too big to be embedded in relatively thin skin. Nevertheless, a thin sensor based on strain gauges is described, for example, in [26], yet small-sized analog-to-digital converting chips for strain gauges are currently not available. In the WENDY robot,[27] the MAC hand,[28] the Robonaut 2 hand [29] and the fingertips of TWENDY-ONE,[6], the external force acting on a link (e.g. arm or finger phalange) can be sensed by a F/T sensor installed on that link. These sensors, however, are not compliant, some require remotely installed digitization electronics and only the summation of all the forces acting on the link can be sensed. Nevertheless, an implementation of four tri-axial sensors in a robotic fingertip is presented in [30]. Moreover, 3-axis F/T sensors were also integrated in the soft skin of the robot Macra.[23]

Capacitive sensors have preferential sensor characteristics such as high sensitivity, yet they often have severe hysteresis.[1] In [31,32] a bump was added on top of an array of four capacitive sensors to make the array sensitive to shear forces; a tiltable plate above the sensors was used in [33]. Capacitive sensor that can measure the shear forces without a bump or plate is suggested in [34,35], but the skin does not include the measurements electronics and therefore the integration into large-scale skin is not straightforward. Recently, CDC chips, such as the AD7147 from Analog Devices, became available.[36] This chip enables digitization of capacitance in very limited space and has been previously used for robotic skin sensing.[5,8] A capacitive sensor that uses copper beryllium ($CuBe_2$) plates was first implemented in [11]. However, the sensors in [5,8,11] can measure only normal force, while the current paper aims to measure also the tangential forces. Furthermore, compared to [11], the shape of the $CuBe_2$ plates was changed to foster a parallel deformation,[12] and in [11] the sensors are embedded in a rather hard casing, while the sensors described in this paper are embedded in soft silicone.

3. Description of the sensor

3.1. The concept of the proposed sensor

For the proposed skin sensor, four capacitive-type force sensing units are tilted in different directions, as can be seen in Figure 1. By covering the sensor with a soft material such as silicone rubber, and angling these units up in four different directions, they should be able to sense and distinguish the shear forces exerted on the upper skin surface. The concept of shear force detection can be found in Figure 1.

For each tilted force sensing unit, two copper beryllium ($CuBe_2$) plates with a bump [12] are used as a double-sided force sensing unit (as one force sensing unit consisting of a copper beryllium plate and a copper foil located on one side of the PCB). The capacitance changes according to the displacement of the $CuBe_2$ plates relative to the PCB caused by the input force. This double-sided capacitor can potentially enhance the sensitivity of the sensor with respect to a single-sided capacitor.[37] $CuBe_2$ has been used for capacitive force sensors and has already proven its advantages of having high strength, excellent spring property, as well as high conductivity.[11,12] A bump (the cylindrical extrusion of the copper beryllium seen in Figure 1) was added to foster the parallel deformation of the copper beryllium to enhance the sensitivity/range of the sensor.[12] For clarification, we expect the bending angle to change when force is applied to the sensor, which is expected to influence the sensor measurements. We assume that the effect on the measurements can be cancelled with careful calibration.

3.2. The circuit of the sensor

As can be seen from Figure 2, one sensor is composed of four force sensing units (S_1–S_4). Each unit consists of a set of capacitive force sensing transducers which are located in the front and the back side of the flexible PCB and both transducers electronically connect to the same signal trace. The resting distance of the copper beryllium and the copper foil is due to the thickness of the solder resist of the flexible PCB, which is 24 μm according to the specifications of the PCB producer. The copper foil is not covered with solder resist, and therefore in the case of overload the copper beryllium plate touches the copper foil, generating a certain signal, which can be used to detect overload, and which is not harmful to the sensor.

The sensor uses an AD7147 chip to digitalize the changes in capacitance of all transducers on the PCB itself which reduces the noise affecting the analog signal trace. The converted data can then be read through an I2C bus that allows four sensor modules (with four force sensing units each in the current implementation) to

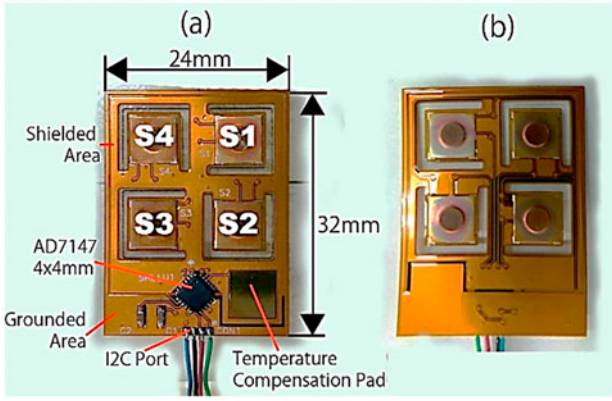

Figure 2. (a) The top view of the flexible PCB showing the four sensing units. (b) The back of the flexible circuit board showing additional four copper beryllium plates attached on the back side of each unit.

share the same data line. This drastically reduces the number of wires when an array of these sensors is implemented on a robot.[8] The AC shield of the chip surrounds the sensing units, which is again surrounded by ground to minimize cross coupling noise (stray capacitance). Moreover, a temperature compensation pad (TCP): a pressure-insensitive capacitive sensor is used to counteract the sensor's susceptibility to temperature change, as has been done previously.[5,12]

3.3. *Soft skin molding process*

The sensor is molded inside a soft material to create the desired soft skin sensor with angled force transducers. Since material selection is not in the scope of interest of this work, Ecoflex Supersoft 30 (from Smooth-On) is used due to its availability as a high strain material. It has a shore hardness of 00-30 which is softer than human skin. While the ideal hardness depends on the application and encountered force limits, softness in general is beneficial, as described in the introduction, yet causes problems for the sensor characteristics. Therefore, Ecoflex Supersoft 30 was purposely chosen, to test how the sensor works in a soft skin (Ecoflex Supersoft 10 is even softer with a shore hardness of 00-10, but has an oily film on the surface even after curing).

The molding process is shown in Figure 3. In order to bend the sensor units to approximately 45° while being embedded in silicone, 45-degree triangular supports made out of the same silicone rubber were molded first with a 3D printed plastic mold. This angle was chosen to allow for a good balance of sensitivity for shear and normal forces. The flexible PCB was positioned in another 3D printed rectangular plastic mold using thin double-sided tape. The molded support was then inserted under the transducer as seen in Figure 3(d) but due to the springback of the flexible PCB, instead of a 45° angle a 30° bending angle was achieved, as measured by a protractor. For the current version of the sensor, we used this 30° bending angle. Future work will include the study of the influence of the bending angle on the measurements and the optimization of the bending angle. After all the sensing elements were supported, the whole sensor is covered under liquid silicone rubber that was then allowed to cure for 4 h during which it also bonds to the triangular support silicone. Finally, the cured skin sensor with the thickness of 7 mm was taken out of the mold. The thickness of 7 mm was chosen in order to cover the whole transducer and have a roughly 2 mm thick layer of silicone on top to increase the robustness and softness (with possible detrimental effects on the sensor performance). In addition to the optimization of the bending angle, the thickness of the silicone above the transducers will also be optimized as future work.

4. Experimental evaluation of the sensor performance

4.1. *Experimental set-ups*

A Signal-to-noise ratio (SNR) test, accumulated load test and temperature drift test were done both before and after the sensor was covered in silicone (Sections 4.2 and 4.3, respectively) to determine and compare the sensor characteristics. During all the experiments, the sensor was connected (I2C bus) and powered by an Arduino Due, and the sensor readout was recorded at 40 Hz sampling rate onto an SD card mounted to the Arduino. The four force sensing units were left lying coplanar with the surrounding circuit board, as shown in Figure 2.

Figure 4 shows the measurement set-up for the SNR test and accumulated load test. The former aimed to find the SNR value of the sensor, while the latter test aimed to determine non-linearity and hysteresis levels of the sensor. The known weights were placed on a weight placement plate with a ⌀6 mm shaft to push on the ⌀3 mm bump of each force sensing unit of the PCB which rest on the flat platform. The shaft goes through a linear bushing which allows the weight to be transferred only in the vertical direction.

Since capacitive sensors are known to be affected by temperature changes and copper beryllium has a high thermal conductivity, a temperature drift test aimed to study the thermal drift occurring in the sensing unit and to test the feasibility of the TCP to counteract the drift. A system as shown in Figure 5 was used to control the heating inside a quartz-glass-tube oven and cooling was achieved through low room temperature. A simple temperature PID controller was used to control the oven to achieve desired temperature via a solid-state relay. As a reference, a temperature sensor (TMP102 from Sparkfun)

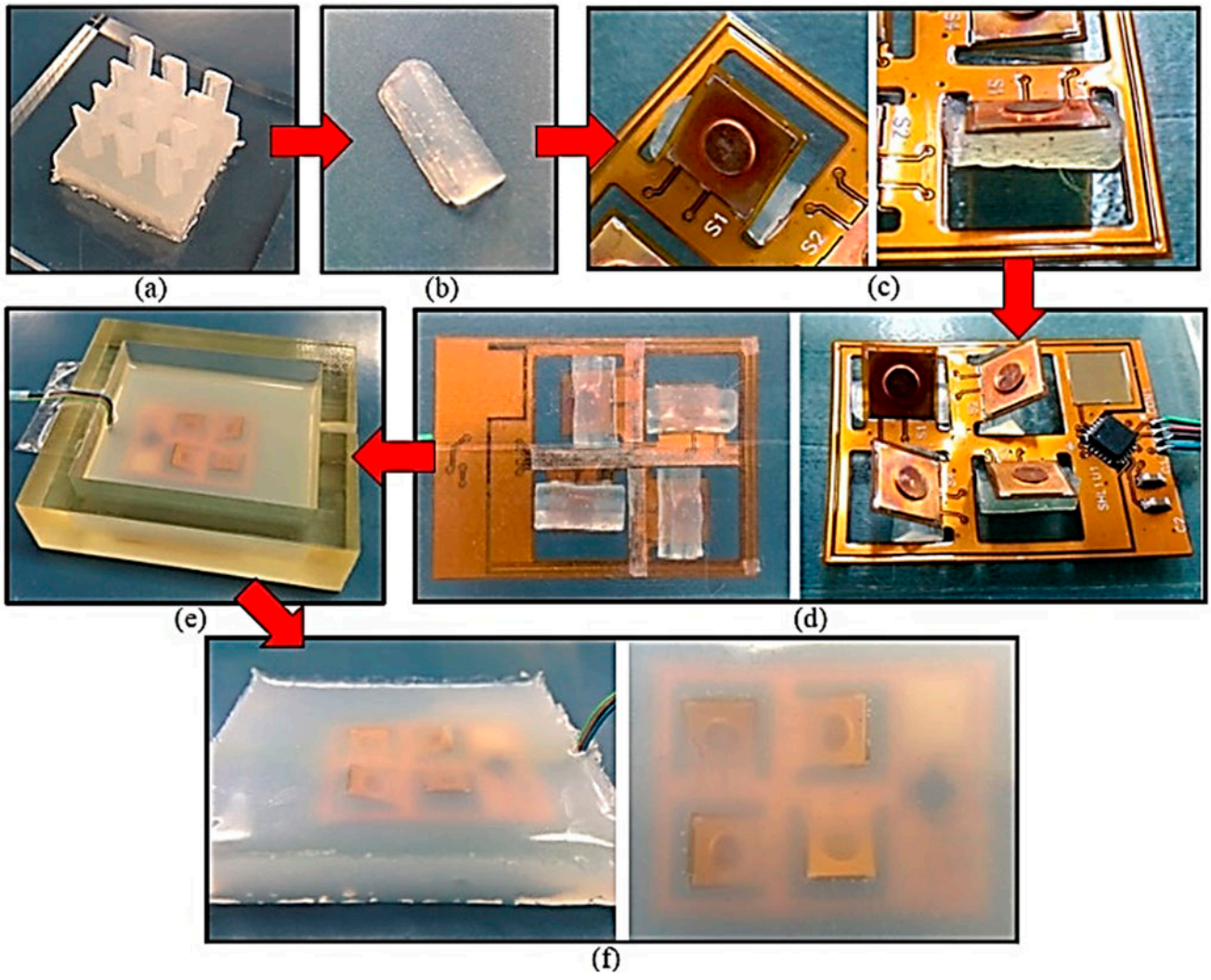

Figure 3. The molding process of the proposed skin sensor: (a) The molded triangular supports. (b) One triangular support. (c) The support is inserted under the tilted transducer. (d) The sensor after all transducer have been tilted up and supported by the triangular supports. (e) The sensor is being covered by liquid silicone rubber inside the 3D printed plastic mold. (f) The sensor after it has been taken out of the mold.

and a humidity sensor (HIH6130 from Sparkfun) were placed only several millimeters away from the capacitive sensor.

Furthermore, four additional tests were done with the molded sensor for evaluating its tri-axial force detection. These tests are to calibrate normal force sensing, to calibrate shear force sensing, being pushed simultaneously by x and y shear forces, and being pushed at varied ratios of normal and shear force. The last two tests were to validate the calibrated force vector detection. The tri-axial force detection set-up as shown in Figure 6 consists of a vertical force generating unit which is mounted on the vertical axis of a manually operated 3-axis stage. The force generating unit is composed of a VM5050-190 linear voice coil motor from Geeplus (called VCM hereafter), a 6-axis force-torque sensor (Nano1.5/1.5 from BL Autotech), a linear bushing, an aluminum shaft that connect VCM's shaft to the force-torque sensor, and a 30-by-30 mm acrylic push plate which is mounted to the end of the force-torque sensor for pushing on the skin sensor. The size of the plate is chosen to cover all the sensing units, allowing all units to be pushed at the same time.

The force exerted by the VCM was controlled by a motor driver (LMD18245 from Texas Instrument); by regulating the current feed to the motor; the force produced by a VCM is proportional to the applied current. The current command and the direction of motion were given by the Arduino Due. The actual forces and torques were sensed by the force-torque sensor and read by an

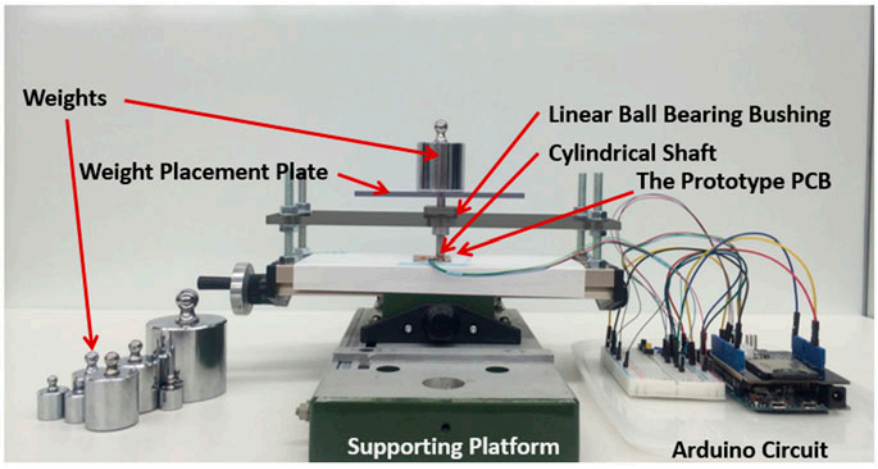

Figure 4. The test set-up including the recording circuit using Arduino Due.

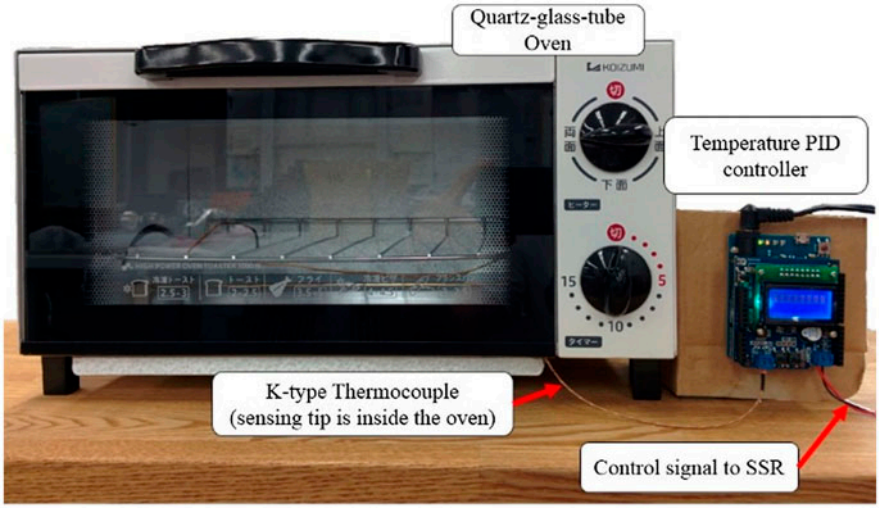

Figure 5. The experiment set-up for the temperature test including quartz-glass-tube oven, K-type thermocouple, solid-state relay and temperature PID controller.

Arduino Uno. Two microcontrollers were used because of the different voltage levels of the skin sensor (3.3 V) and the 6-axis force-torque sensor (5 V) (the VCM is powered with 24VDC). The actual forces and the read-outs of the sensor were recorded into a SD card on each Arduino with synchronized sampling rate of 40 Hz. The synchronization of the two sensor readings was verified with an oscilloscope.

In the normal force calibration, the molded skin sensor was placed in a 3D printed hard-plastic block and the block was then mounted to the top of the *x*–*y* stage with step clamps. In the shear force calibration, the push plate was changed to a plate which had a 45° alignment with the axis of the push unit, and an acrylic adjustable angle stage was used to position the skin sensor at 45° (refer to Figure 7). Therefore, the vertical force generated by the VCM was decomposed into normal and tangential forces acting on the sensor's surface. Additionally, by rotating the sensor on the surface of the tilted stage, the multi-directional shear force can be generated. The axes of the sensor and its origin are defined as shown in Figure 8. In the *x*–*y* shear push test, a new 3D printed plastic block as shown in Figure 9 was used to hold the skin sensor. With this block, the shear force acting in both *x*- and *y*-directions can be generated simultaneously. In the last test, the adjustable angle stage was altered to 30° and 15° in order to change the proportion of the normal force and shear force acting on the proposed sensor (the push plates having the same angle were used correspondingly (refer to Figure 10)).

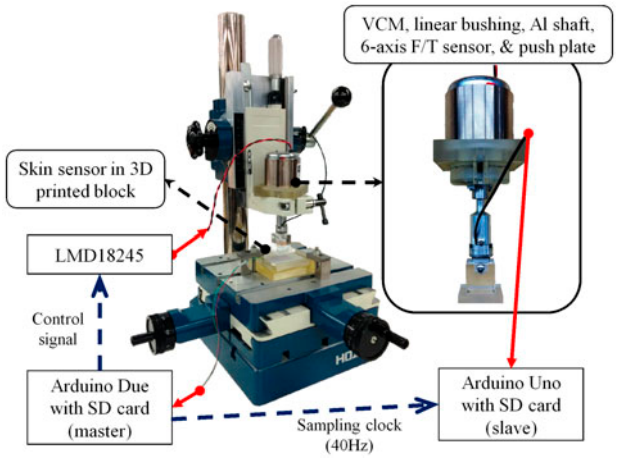

Figure 6. The experimental set-up of the tri-axial force test.

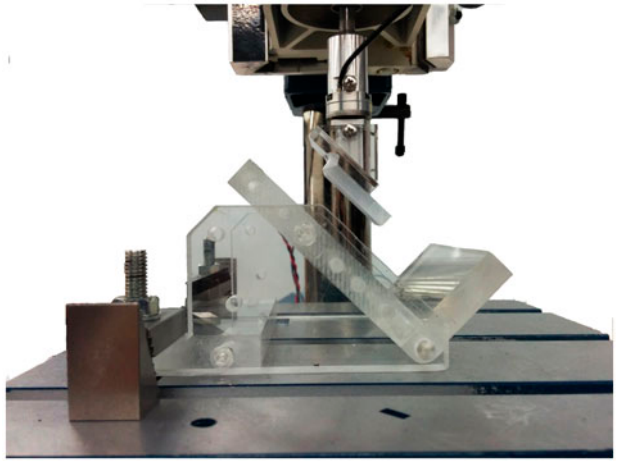

Figure 7. The adjustable angle stage fixed at 45° with respect to the *x-y* stage surface and the corresponding 45-degree push plate.

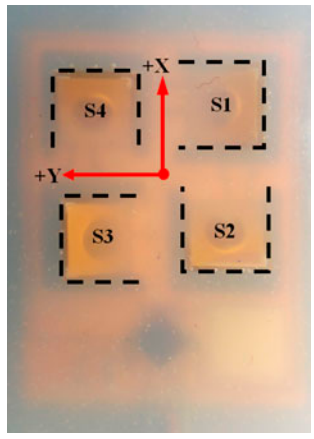

Figure 8. The location of the four force sensing units, and the axes and origin of the skin sensor are shown.

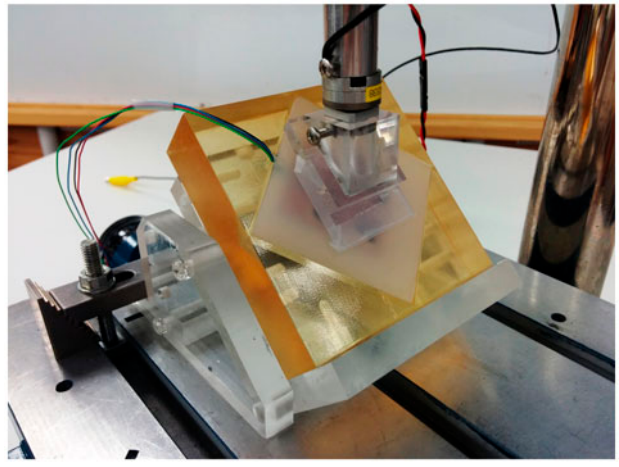

Figure 9. A 3D printed plastic block that allow the sensor to be aligned at 45° with respect to the outer edge of the block. This allows the shear force to act in both *x* and *y* directions at the same time.

4.2. *Pre-mold experiments*

4.2.1. *SNR test*

In this test, one sensor unit was loaded with a certain fixed weight per trial. The weights were placed on one sensor bump for approximately 5 s, and the response of the sensor is recorded. Four weights of 50 mg, 250 g, 500 g, and 1250 g were used in this experiment. Ultimately, the sensor values before and during loading were used to obtain the SNR, which is calculated according to Equations (1) or (2).[38]

$$\mathrm{SNR} = \frac{|\mu_U - \mu_P|}{\sigma_u} \tag{1}$$

$$\mathrm{SNR_{dB}} = 20\log_{10}\left(\frac{|\mu_U - \mu_P|}{\sigma_u}\right)\mathrm{dB} \tag{2}$$

where: μ_U = mean value of sensor when not loaded; μ_P = mean value of sensor when loaded; and σ_u = standard deviation of value when not loaded.

The results for all transducers can be found in Table 1. The SNR increases with higher load as expected. The SNR value of S_2 when loaded with 250 g is 3627.24 (71.19 dB), which is relatively high for this kind of sensor, compared, for example, to the SNR of 315 (49.97 dB) found in [11] at the load of approximately 306 g. Furthermore, the transducer has a high level of sensitivity and can apparently sense the load of 50 mg.

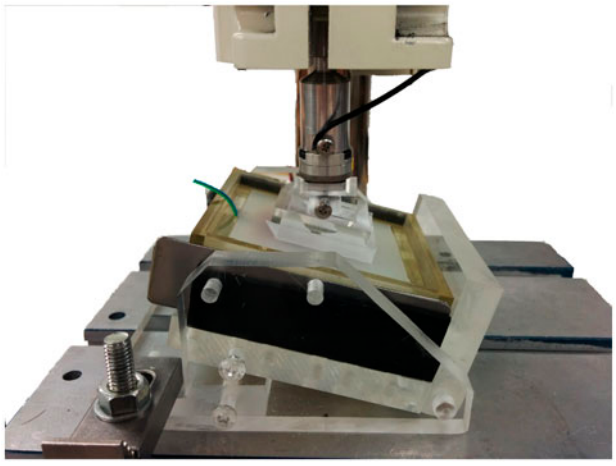

Figure 10. The adjustable angle stage is set at 15° with respect to the *x-y* stage surface and the corresponding 15-degree push plate.

The value of S_1 drops to zero under 1250 g load which corresponds to overload. Despite being overloaded, the sensor still functions normally afterwards, which indicates that the proposed sensor is able to withstand excessive load without losing its functionality. The hard limits of the sensor should make it robust to overload, however more overload tests will be performed in the future.

4.2.2. *Accumulated load test*

In this test, known weights as described in Table 2 were sequentially loaded on and taken off one bump of a force sensing unit in a last out, first in (LIFO) fashion with a 5-s interval per step.

Figure 11 shows the sensor readout of S_3. For each step, the sensor measurement slowly and gradually changes, which is most obvious for step 17, for which also the highest change between steps occurs (500 g). As can be expected, some hysteresis can be observed. In particular, for the 753 g load, there is a difference of 853 digits when comparing loading and unloading, which corresponds to about 42 g according to the calibration with quadratic curve fitting.

The response of S_3 to both the loading and unloading sequences is shown in Figure 12. Also, the quadratic approximation lines for the loading and unloading are drawn to show the nonlinear behaviour of the sensor. The results for the other sensor units (S_1, S_2 and S_4) were similar to the one shown here. Moreover, the hysteresis can also be seen. By using Equation (3), the hysteresis percentage of S_3 was 0.37% of the maximum load of 1253 g.

$$\text{Hysteresis } \% = \left| \frac{(F_{\text{mu}} - F_{\text{ml}})}{(F_{\text{max}} - F_{\text{min}})} \right| \times 100\% \qquad (3)$$

where F_{ml} and F_{mu} were the converted force values of the loading and unloading cycles taken at the midpoint weight of (1253 g − 0 g)/2 = 626.5 g.

4.2.3. *Temperature drift test*

The circuit board was exposed to varying temperatures, starting from 15 °C and gradually increased to 40 °C, and then brought back to 15 °C. During this process, the values of S_1, S_2, S_3, S_4 and TCP were recorded.

The result shows that the measurements of the force sensing units and the TCP follow the profile of the temperature. Therefore, the drift of the TCP can be used to cancel the thermal effect on the force sensing transducers by using Equation (4),

$$\widehat{S}_i(t) = S_i(t) - K_i \times \text{TCP}(t) \qquad (4)$$

where $\widehat{S}_i(t)$ is the value of the sensor i at time t after being compensated, and $S_i(t)$ is the raw value recorded from the same sensor at time t. $TCP(t)$ is the value taken from the TCP at time t. Lastly, K_i is the gain factor estimated for calibration purposes, set differently for each sensor. This method has been used successfully previously.[5,12] The compensation was successful; the drift was reduced from 10 to 5 g.

4.3. *Post-mold experiments*

4.3.1. *SNR test*

This test was done in the same fashion as in Section 4.2.1 but the weights of 8.7, 250, 500 and 1250 g were used in this test. The 50 mg weight was replaced by the 8.7 g

Table 1. The comparison of the SNR_{dB} value of each sensing element before and after the molding.

	S_1		S_2		S_3		S_4	
Weight (g)	Pre	Post	Pre	Post	Pre	Post	Pre	Post
0.05	13.78		18.62		25.93		17.73	
8.7		34.47		22.42		20.72		23.32
250	78.78	54.45	71.19	48.89	70.71	54.97	61.87	48.84
500	88.75	61.83	76.90	56.89	76.46	62.42	73.63	56.28
1250		78.98	85.78	75.43	89.04	73.99	86.32	78.84

Table 2. The list of weights which will be put on a single force sensing unit during the accumulated load test at each step. The loading sequence goes from 0 to 17 and the unloading sequence goes from 17 to 0.

Step	0	1	2	3	4	5	6	7	8	9	10	11	12	13	14	15	16	17
Weight (g)	0	45	46	48	53	63	73	93	113	133	153	203	253	353	453	553	753	1253

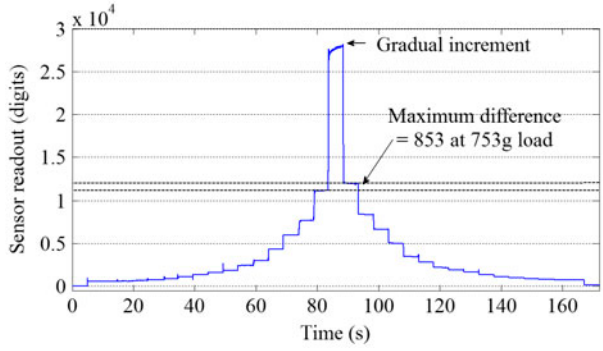

Figure 11. The relationship between time and sensor readout of S_3 during the accumulated load test before molding.

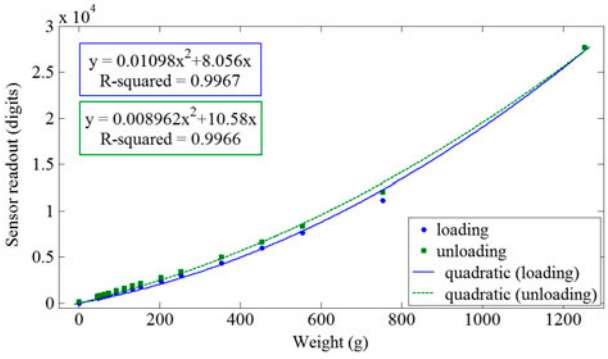

Figure 12. The relation between the weights loaded on S_3 and the sensor readout of S_3. The values for the quadratic approximation are shown in the blue box for loading and in the green box for unloading.

shaft because the 50 mg weight could not be sensed by the molded sensor. Furthermore, with the shaft, the weight could repeatedly be placed in the same location.

All results are shown in Table 1. As expected, the SNR are higher when the load increases, and the SNR values are lower after the molding compared to before the molding. This might be due to the fact that the load that was applied on the sensor surface above a transducer was distributed not only to the element underneath, but also to the surrounding silicone and to the other sensing elements as well as can be observed in Figure 13. This is further supported by the fact that the post-mold S_1 could sense the load of 1250 g.

4.3.2. *Accumulated load test*

This test was performed in the same fashion as in Section 4.2.2. The weights were sequentially added and taken off in a LIFO fashion following the sequence shown in Table 2.

Figure 14 shows the sensor readout of S_3. At each step, the sensor readout slowly and gradually changes, most obviously at step 17, where the highest weight change between steps occurs (500 g). Compared to Figure 11, the transient response time of the molded sensor was drastically longer which we expect is due to the viscoelasticity of the silicone. Again some hysteresis can be seen, especially at the 753 g load of around 41 g difference when comparing loading and unloading. The difference in grams was obtained in the same fashion as Section 4.2.2.

The response of S_3 to both the loading and unloading sequences is shown in Figure 15. Comparing to Figure 12, it can be seen from the higher R^2 values that the result here is closer to the quadratic approximation lines both when loading and unloading. Moreover, it can be seen that the response after the molding is about 7.5 times less compared to pre-molding. This is due to the fact that the load is distributed to the silicone rubber and the other sensors as explained above and shown in Figure 13.

Furthermore, by using Equation (3), the hysteresis percentage of S_3 was 1.27% of the maximum load of 1253 g, while that of the pre-mold was 0.37%. Nevertheless, we expect that the hysteresis (and also the difference between the transducers) can be reduced with an

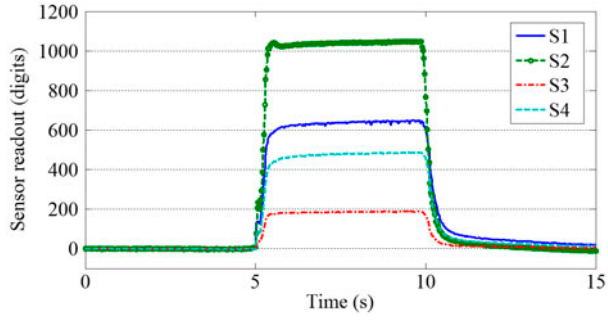

Figure 13. The post-mold step response of all sensing elements when the load of 250 g is applied to S_2. It can be seen that the load is also sensed by the surrounding sensor units.

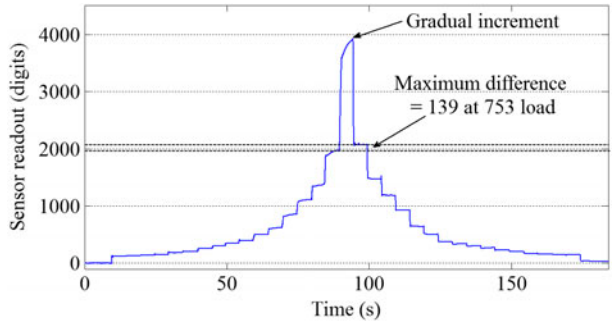

Figure 14. The relationship between time and sensor readout of S_3 during the accumulated load test after molding.

improved version of the PCB, which will be discussed in the Future Work section.

4.3.3. *Temperature drift test*

With the same method used in Section 4.2.3, the result of the experiment is shown in Figure 16. By using Equation (3) but with new constants K_i, the compensation of the thermal drift can be accomplished as shown in Figure 17. The drift can be reduced from around 260 to 54 g. Compared to the pre-mold result, the drift band is bigger but is also attenuated more significantly as well. The cause of the higher residual drift (in digits as well as in gram) might be the force transducers located higher to the surface than the TCP, which was still located at the bottom of the skin. This could lead to a different temperature distribution in those two locations. Nevertheless, the TCP measurements are more related to the sensor measurements S_1, S_2, S_3 and S_4 than the TMP102 temperature sensor just a few millimeters away from the sensor. Further possibilities of drift compensation will be discussed in the future work section. Finally, the humidity sensor measurements of both pre- and post-mold are

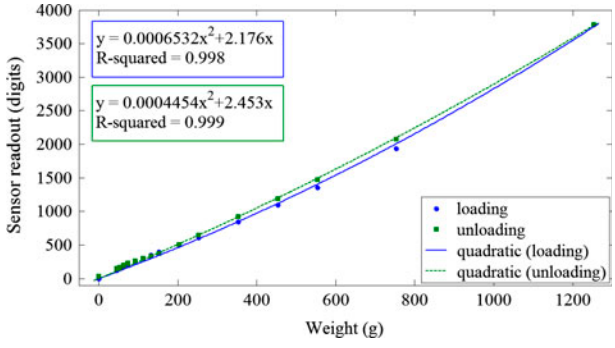

Figure 15. The relationship between the load and sensor readout of S_3 after the molding and its quadratic approximation line of both loading and unloading sequences. The values shown in the blue box are for loading and those in the green box are for unloading.

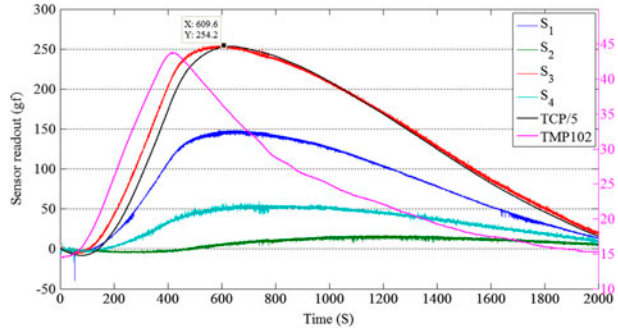

Figure 16. The thermal drift of all sensing units after the molding including TCP (gray, scaled down by five) are shown together with the actual temperature (purple) sensed by the TMP102 sensor.

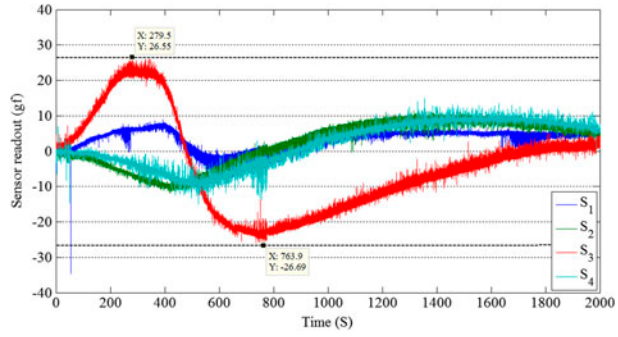

Figure 17. The sensor readout of all four transducers after the temperature compensation.

nearly identical and are inversely proportional to the temperature.

Additionally, the sensor was also left in the room temperature, around 26–27 °C, for 30 min and the sensor readout was monitored together with the actual temperature and humidity. This was done to verify whether the use of the TCP to compensate thermal drift is valid also in the condition that the temperature only slightly changes. The pre-compensated data of all sensors, TCP and the actual temperature are shown in Figure 18. It can be seen that the readouts slowly drift as the temperature changes, and there was a slight variation in the drift among the sensors. Again, the TCP data was used to compensate for the drift. The same gain found previously was used and the result of the compensation can be seen in Figure 19. The drift could be reduced from 8 to −4 g.

4.3.4. *Tri-axial force test*

4.3.4.1. Normal force calibration. The experiment was conducted by continuously pushing the sensor vertically with six equally spaced steps of forces which the VCM can generate, which ranges from around 340 to 1440 g.

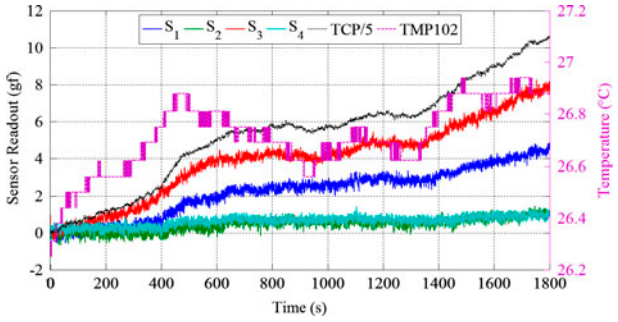

Figure 18. The thermal drift of all sensing units when subject to the slightly changed temperature and TCP (gray, scaled down by five) are shown together with the actual temperature (purple) sensed by the TMP102 sensor.

Each step lasted for 10 s. Then the force was increased at the end of each step.

The test was repeated four times, all collected data were filtered with a Savitzky–Golay filter. The sensor's readout and the forces sensed by the force-torque sensor are shown in Figure 20(a) and (b), respectively; the different response of each sensing unit to the same force can be clearly seen. The calibration of each sensing unit with respect to the vertical force F_z is done by firstly dividing the F_z by four considering that the force is equally distributed to all four sensing units. A quadratic polynomial was then used to convert the ith sensor measurements $S_i(t)$ in digits at time t to force $F_i(t)$ in gram.

$$F_i(t) = a_i S_i(t)^2 + b_i S_i(t) \tag{5}$$

The coefficients a and b of each sensing unit were computed by using all of the collected data excluding the 1st second of each push in order to remove the transient response. As a result, four quadratic functions were constructed with averaged root-mean-square error (RMSE) of 5.8035 g and averaged R^2 value of 0.9776.

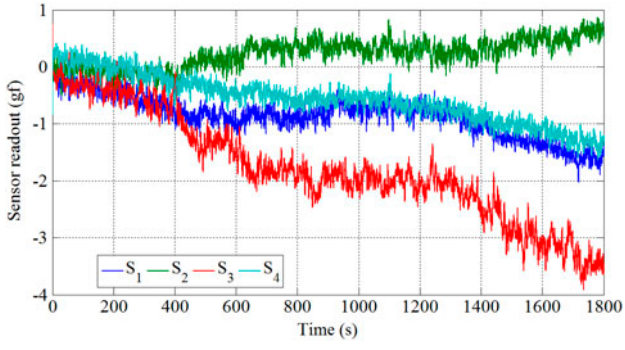

Figure 19. The sensor readout of all four transducers after the temperature compensation when the temperature slightly changed.

The result of the calibration is shown in Figure 20(c). It can be seen that the readouts are close to each other. Moreover, the summation of all calibrated readouts is mostly identical to F_z as can be seen in Figure 20(d) with a RMSE value of 21.69 g.

4.3.4.2. Shear force calibration. This test was performed in the same fashion as the previous test; the VCM exerts vertical force on the sensor's surface. The same six steps of incremental forces were applied on the sensor for a 10-s interval per step. However, this time, the test with shear force acting in each direction ($+x$, $-x$, $+y$, $-y$) was repeated four times. All collected data was then filtered with a Savitzky–Golay filter and then converted into force values by using their corresponding quadratic equations obtained from the previous experiment.

The resultant force sensed by each sensing unit when the shear force was acting in each direction is shown in Figure 21. It can be seen that the transducer that points in the same direction as the shear force sensed higher forces, while the transducer that points in the opposite direction sensed lower forces when compared to the average of all sensing units. The forces sensed by the other two units which point in the direction perpendicular to the shear force were close to the average line. Moreover, it can also be seen that the increment and the decrement of force sensed by the two units which are parallel to the shear force direction had relatively the same magnitude of change. This pattern of response can be used to decompose a force vector into normal and shear force components.

Subsequently, the result of this experiment was used to determine the coefficients of the following equations in order to allow the sensor to measure an arbitrary force vector.

$$F_{x,\text{skin}}(t) = a_x(F_4(t) - F_2(t)) \tag{6}$$

$$F_{y,\text{skin}}(t) = a_y(F_3(t) - F_1(t)) \tag{7}$$

A linear function was used for acquiring the equation for each axis of force. The linear curve fitting was done by firstly excluding out the 1st second and the 10th second of each step of push to eliminate the transient-state data. The data of $+x$ and $-x$ shear forces were used to determine a_x and $+y$ and $-y$ shear force's data were used to calculate a_y. As a result, the coefficients a_x and a_y were calculated with RMSE values of 42.33, 42.60 and 27.07 g, and R^2 values of 0.9820, 0.9836 and 0.9958, respectively.

Furthermore, to demonstrate the ability of force vector detection, a plot between calculated force vector and one of the actual force data (used during the calculation of a_x, and a_y previously) with $+x$ shear component is shown in Figure 22 with RMSE values of 33.00, 39.54

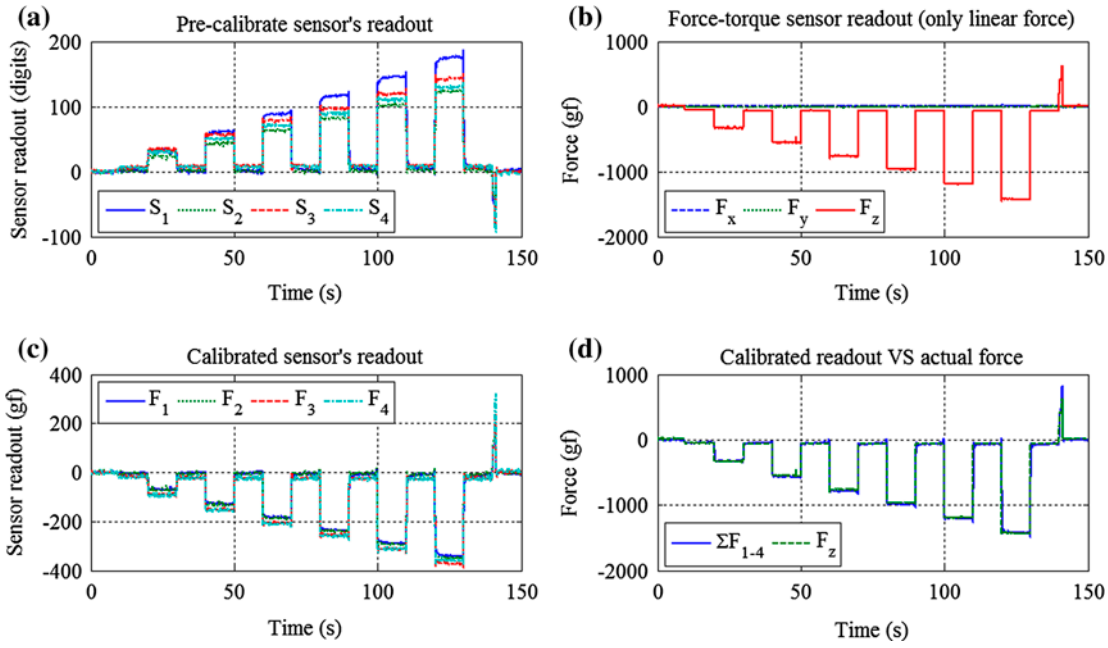

Figure 20. The result of the sensor calibration experiment; (a) pre-calibrate sensor's readout (b) force-torque sensor readout (only linear force) (c) calibrated sensor's readout (d) the comparison between converted sensor's readout and actual force readout.

and 18.24 g for $F_{x,\text{skin}}$, $F_{y,\text{skin}}$ and $F_{z,\text{skin}}$, respectively. It can be seen that $F_{y,\text{skin}}$ is the least accurate, while $F_{z,\text{skin}}$ is the most accurate. On the other hand, when comparing the force calculation when applying $+y$ shear force, $F_{x,\text{skin}}$ becomes the least accurate. Moreover, it can be seen that the sensor is more sensitive to normal force than shear force. This could be due to the PCB bending angle of 30°; hence, the sensor is more affected by the normal force component.

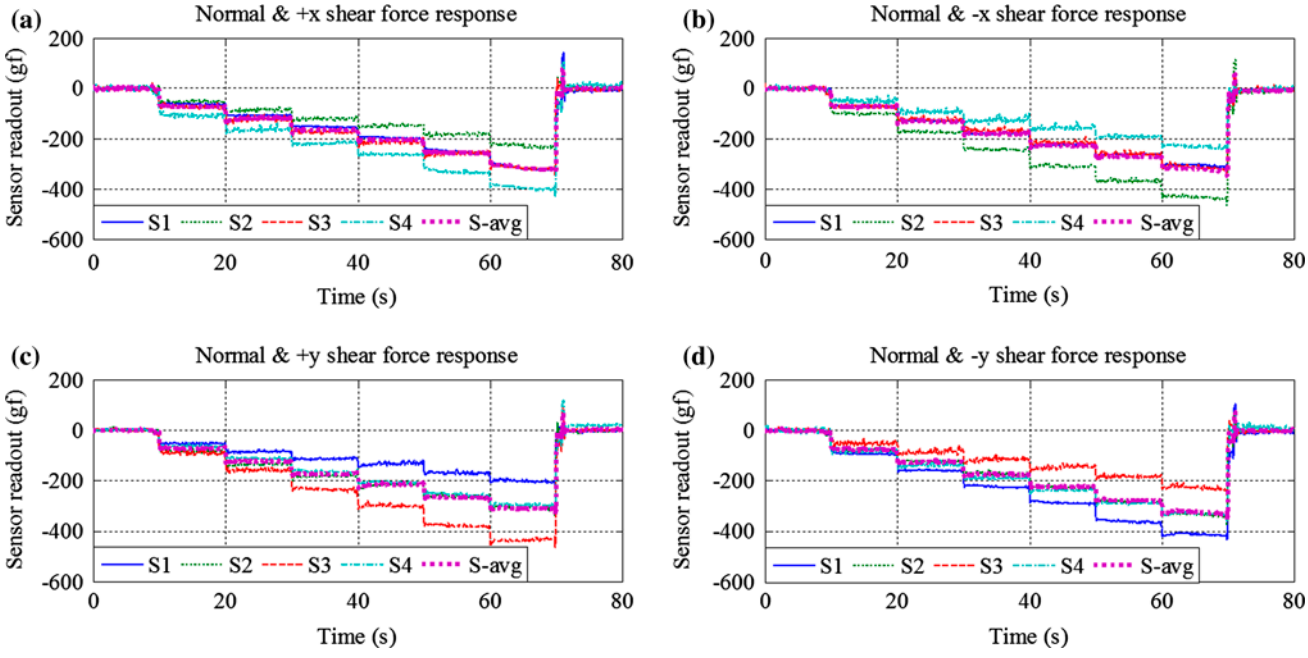

Figure 21. The resultant force sensed by all four units when being pushed with normal and shear force acting in different directions. (a) with $+x$ shear force (b) with $-x$ shear force (c) with $+y$ shear force (d) with $-y$ shear force.

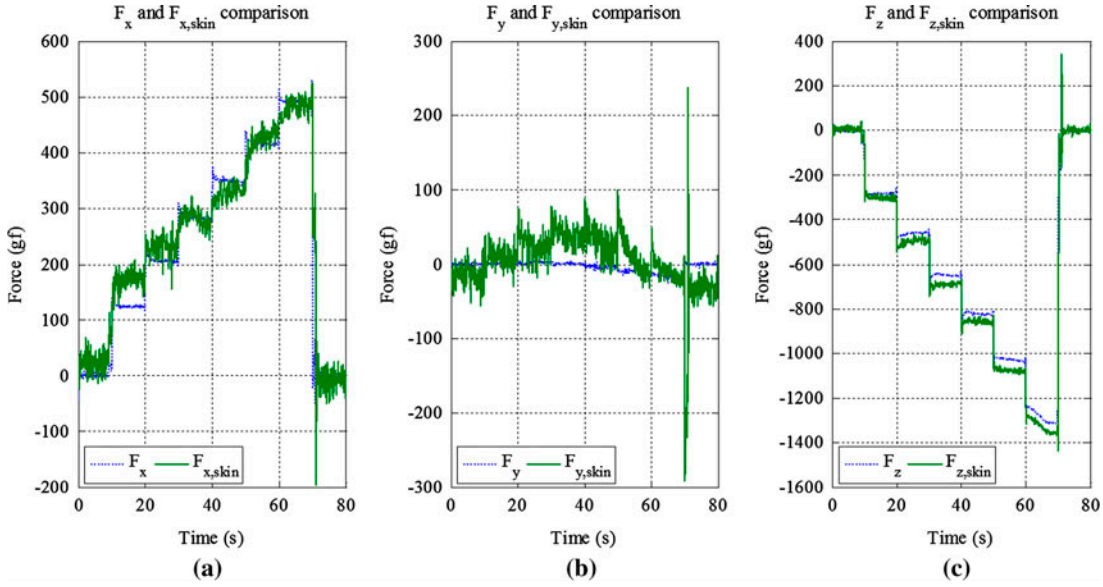

Figure 22. The comparison between the calculated force vector and the actual force vector when normal force and $+x$ shear force is applied. The adjustable angle stage is set to 45°.

4.3.4.3. x–y *shear force push.* The block shown in Figure 9 was used. The same pattern of pushing of the force generating unit as in the previous experiment was used.

In this test, normal force and shear force acting in four directions; $+x+y$,$+x-y$, $-x+y$, and $-x-y$ directions were exerted on the sensor in this experiment. The result of pushing the sensor with shear force in the direction of $+x+y$ can be seen in Figure 23 with RMSE values of 24.41, 31.98 and 20.74 g, while the averaged RMSEs of all 4-direction shear tests are 36.01, 38.69 and 19.93 g for $F_{x,\mathrm{skin}}$, $F_{y,\mathrm{skin}}$, and $F_{z,\mathrm{skin}}$ respectively.

4.3.4.4. 30° and 15° pushes. The stage was adjusted to 30° and 15° and the block as in Sections 4.3.4.1 and 4.3.4.2 was used. At each angle setting, the sensor was pushed in four directions of shear force, namely $+x$, $-x$, $+y$ and $-y$ directions with their corresponding push plates having the same angle (refer to Figure 10). Again,

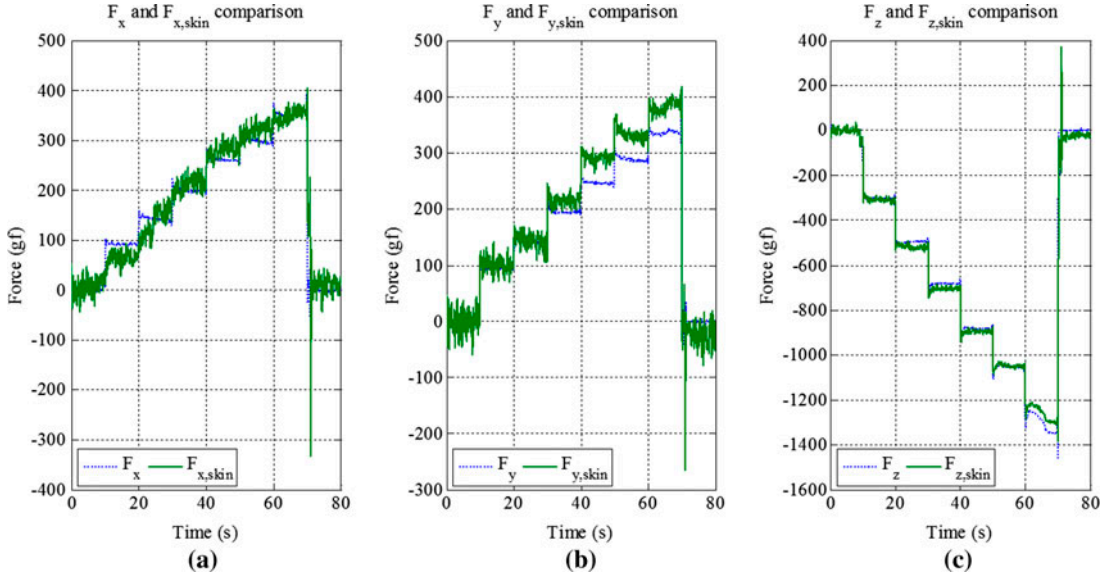

Figure 23. The comparison between calculated force vector and the actual force vector when the normal force and $+x+y$ shear force is applied. The adjustable angle stage is set to 45°.

Table 3. The comparison of the force vector calculation's accuracy at all experiments in tri-axial force test section.

Experiment		RMSE			R^2		
		$F_{x,\text{skin}}$	$F_{y,\text{skin}}$	$F_{z,\text{skin}}$	$F_{x,\text{skin}}$	$F_{y,,\text{skin}}$	$F_{z,\text{skin}}$
Calibration at 45°		41.7728	34.3551	24.9617	0.93878	0.93882	0.99618
With both x & y shear		36.0068	38.6854	19.9335	0.88953	0.86793	0.99721
Varied normal & shear ratio	30°	49.6397	25.4368	38.7147	0.73647	0.90931	0.9905
	15°	38.2085	29.3996	46.9959	0.43489	0.64024	0.98067

the same pattern of pushing of the force generating unit as in the previous experiment was used.

The comparison of the force vector calculation's accuracy in various experiments is shown in Table 3 as the values of averaged RMSE and R^2 for each axis at each test. When the pushing angle decreases, the ratio of shear force to normal force decreases too. According to the result when the sensor was pushed at 15° in $+y$ direction, the maximum $F_{y,\text{skin}}$ was only 120 g, while the maximum $F_{z,\text{skin}}$ was 1400 g. Therefore, when less force is sensed at a certain axis, the slightly varied RMSE values could further influence the measurement, resulting in lower R^2 values. Figure 24 shows the result of pushing the sensor at 15° with shear force in the direction of $+y$.

5. Conclusion and future work

This paper presents the design and experimental evaluation of a novel capacitive tri-axial skin force sensor. The implementation was successful, and measuring distributed force vectors directly at the impact sites is possible. Tests before and after the molding process were performed. The following aspects were evaluated:

(1) The main novelty is the tilted capacitive transducers with copper beryllium that enables measuring the tangential forces acting on the sensor surface. Experiments clearly show that the sensor can sense the 3D force vector with a certain level of accuracy. The performance of the force vector detection depends on several factors which will be further studied; the influence of bending angle on the measurement will be explored; the angle and also the silicone layer thickness will be optimized.

(2) Even after the molding, the sensor has a relatively high SNR, comparable to the one published in [11]. In our experiment, the hysteresis was limited within 4% of the maximum force after the molding when covered with a 7-mm-thick layer of Ecoflex Supersoft 30 silicone rubber.

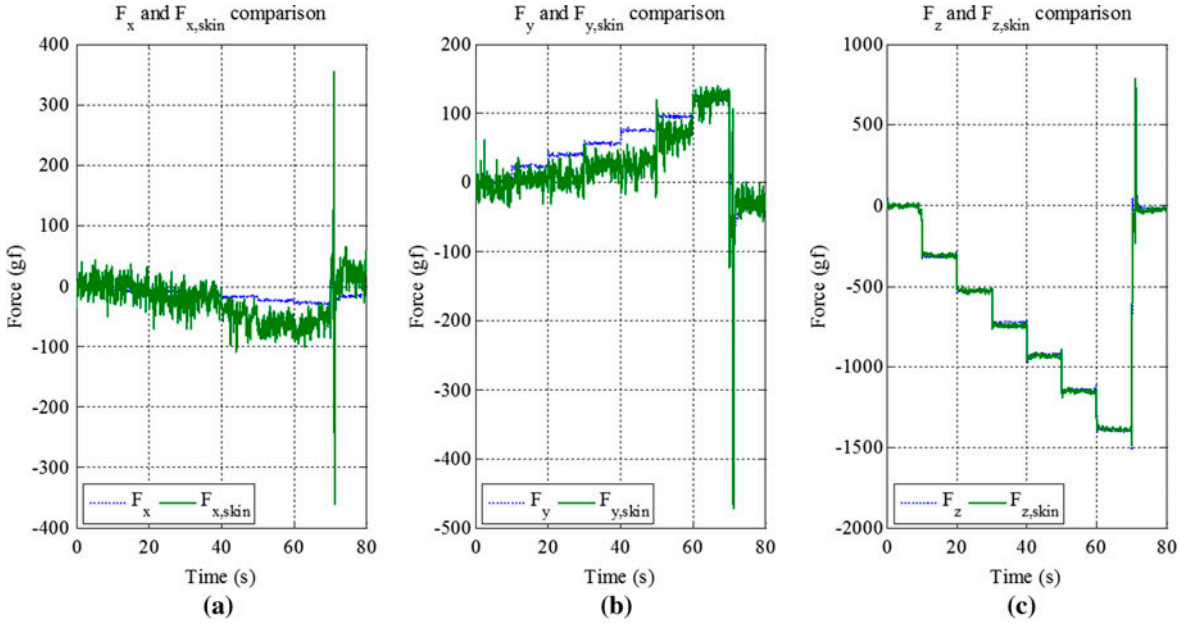

Figure 24. The comparison between calculated force vector and the actual force vector when normal force and $+y$ shear force is applied. The adjustable angle stage is set to 15°.

(3) The TCP can limit the effect of temperature changes on the sensor measurements. To further minimize the influence of the temperature on the sensor measurements, low frequency low amplitude signals can be filtered out, similar to [8].
(4) The molded version of the sensor introduces cross-talk, has higher hysteresis and decreases the sensitivity of the sensor. Such characteristics are to be expected, due to the silicone, and are not catastrophic for our intended use in a humanoid robot. The source of the hysteresis in the unmolded sensor is relatively small, but will be further investigated and can potentially be reduced with an updated version of the flexible PCB or the copper beryllium plates. The hysteresis and cross-talk can only be reduced to a certain extent with the choice of different viscoelastic materials while maintaining the softness of the skin, which is important for the safety property of the skin. Moreover, the thickness of pure silicone above the sensor units could be reduced (it is currently about 2 mm), but the robustness of the sensor has to be taken into account. The sensitivity/range of the sensor units can be changed by the thickness of the copper beryllium plates, and thinner plates can be used to adjust the sensitivity/range suitable for the intended use in a humanoid robot.

Further experimental evaluation is necessary. For example, several instances of the same sensor will be produced and tested to obtain more comparative results. Overload experiments will be done as well.

In future versions of the sensor, multi-layer, partially bonded flexible PCBs will enable the placing of the chip below the transducers, so that the whole surface of the robot can be covered with transducers. Ports on all sides will enable an efficient networking structure with minimal wiring, as in [39].

Disclosure statement

No potential conflict of interest was reported by the authors.

Funding

This work was supported by the JSPS Grant-in-Aid for Scientific Research (S) [grant number 25220005]; JSPS Grant-in-Aid for Young Scientists (B) [grant number 15K21443]; Research Institute for Science and Engineering of Waseda University; and the Program for Leading Graduate Schools, 'Graduate Program for Embodiment Informatics' of the Ministry of Education, Culture, Sports, Science and Technology.

Notes

1. http://www.touchence.jp
2. http://optoforce.com/

Notes on contributor

Sophon Somlor received his Bachelor of Engineering in Mechatronics Engineering from King Mongkut's University of Technology Thonburi, Thailand in 2008 and his Master of Engineering in Mechatronics Engineering from Asian Institute of Technology, Thailand in 2011. He is currently working toward his PhD degree at Waseda University, Japan. His research interests cover various field of robotics. His Bachelor's thesis was to develop a 6-DOF articulated robot arm with his colleagues to perform several pick and place tasks (including pouring water from a plastic bottle). His master's thesis was about developing a single-legged hopping robot using tendon-driven system, spring-loaded leg and electromagnetic clutch. Finally, his recent work is about the development of multi-axis tactile sensor for robotics hands and arms for a safe and reliable interaction with human and environment at Sugano Lab, Waseda University, Japan.

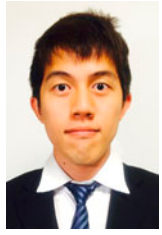

Richard Sahala Hartanto received his Bachelor of Engineering in the Department of Modern Mechanical Engineering from Waseda University in 2015. He contributed in the development of a tri-axial capacitive skin sensor in Sugano Laboratory, which involves circuit design and production methods of the sensor.

Alexander Schmitz received his Master's degree in cognitive science (with honors) from the University of Vienna, Vienna, Austria, in 2007, and PhD degree from the University of Sheffield, Sheffield, England in 2011. The research for his Master's thesis was performed with the Artificial Intelligence Laboratory, University of Zurich, Zurich, Switzerland, where he worked on compliant robotics. He performed his PhD degree as part of a joint location programme with the Italian Institute of Technology, Genova, Italy, where he developed tactile sensors for the hands of the humanoid robot iCub. As a postdoctoral assistant, he worked in the Sugano Laboratory at Waseda University, Tokyo, Japan. He is currently an assistant professor at Waseda University, Tokyo, Japan. His research interests include tactile sensing, compliant robotics, human–robot collaborative movement and robotic object handling.

Shigeki Sugano received his BS, MS and Doctor of Engineering degrees in Mechanical Engineering in 1981, 1983, and 1989 from Waseda University. Since 1990, he has been a faculty member in the Department of Mechanical Engineering at Waseda, where he is currently a professor. Since 2014, he has served as the dean of the School/Graduate School of Creative Science and Engineering, Waseda University. Since 2013, he has served as the programme coordinator of the MEXT Leading PhD Program: Waseda Embodiment Informatics Program. His

research interests include human-symbiotic anthropomorphic robot design, dexterous and safe manipulator design, and human–robot communication. He received the Technical Innovation Award from the RSJ for the development of the Waseda Piano-playing Robot: WABOT-2 in 1991. He received the JSME Medal for Outstanding Paper in 2000. He received the JSME Fellow Award in 2006, the IEEE Fellow Award in 2007. He received IEEE RAS Distinguished Service Award in 2008, the RSJ Fellow Award in 2008 and the SICE Fellow Award in 2011. He received RSJ Distinguished Service Award in 2012. He served as the Secretary of the IEEE RAS in 2006 and 2007. He served as an AdCom member of the IEEE RAS from 2008 to 2013. He served as a director of RSJ in 1995, 1996, 1999 and 2000. From 2007 to 2012, he served as the editor in chief of the International Journal of Advanced Robotics (RSJ). He served as the Head of the System Integration Division of the SICE in 2006 and 2007. He serves as a director of SICE in 2008 and 2009. From 2001 to 2010, he served as the president of the Japan Association for Automation Advancement. He served as a general co-chair of the 2006 IEEE/RSJ International Conference on Intelligent Robots and Systems (IROS2006) and a programme co-chair of the 2009 IEEE International Conference on Robotics and Automation (ICRA2009). He served as the general chair of the SICE2011 in 2011. He also served as the general co-chair of the ICRA2012, and the programme chair of the AIM2012. He served as the general chair of the IROS2013 in Tokyo in 2013.

References

[1] Dahiya RS, Metta G, Valle M, et al. Tactile sensing – from humans to humanoids. IEEE Trans. Rob. 2010;26: 1–20.

[2] Dahiya RS, Mittendorfer P, Valle M, et al. Directions toward effective utilization of tactile skin: a review. IEEE Sens. J. 2013;13:4121–4138.

[3] Kojima K, Sato T, Schmitz A, et al. Sensor prediction and grasp stability evaluation for in-hand manipulation. In: IEEE/RSJ International Conference on Intelligent Robots and Systems. Tokyo (Japan); 2013; p. 2479–2484.

[4] Schmitz A, Bansho Y, Noda K, et al. Tactile object recognition using deep learning and dropout. In: IEEE-RAS International Conference on Humanoid Robots (Humanoids 2014). Madrid (Spain); 2014; p. 1044–1050.

[5] Maiolino P, Maggiali M. A flexible and robust large scale capacitive tactile system for robots. IEEE Sens. J. 2013;13:3910–3917.

[6] Iwata H, Sugano S. Design of human symbiotic robot TWENDY-ONE. In: IEEE International Conference on Robotics and Automation. Kobe (Japan); 2009; p. 580–586.

[7] Cabibihan JJ, Chauhan SS, Suresh S. Effects of the artificial skin's thickness on the subsurface pressure profiles of flat, curved, and Braille surfaces. IEEE Sens. J. 2014;14:2118–2128.

[8] Schmitz A, Maiolino P, Maggiali M, et al. Methods and technologies for the implementation of large-scale robot tactile sensors. IEEE Trans. Rob. 2011;27:389–400.

[9] Jamone L, Natale L, Metta G, et al. Highly sensitive soft tactile sensors for an anthropomorphic robotic hand. IEEE Sens. J. 2015;15:4226–4233.

[10] Ohka M, Tsunogai A, Kayaba T, et al. Advanced design of columnar-conical feeler-type optical three-axis tactile sensor. Proc. Comput. Sci. 2014;42:17–24.

[11] Mittendorfer P, Cheng G. Integrating discrete force cells into multi-modal artificial skin. In: 2012 12th IEEE-RAS International Conference on Humanoid Robots (Humanoids 2012). Osaka (Japan); 2012; p. 847–852.

[12] Somlor S, Schmitz A, Hartanto RS, et al. A prototype force sensing unit for a capacitive-type force-torque sensor. In: 2014 IEEE/SICE International Symposium on System Integration (SII). Tokyo (Japan); 2014; p. 684–689.

[13] Puangmali P, Althoefer K, Seneviratne LD, et al. State-of-the-art in force and tactile sensing for minimally invasive surgery. IEEE Sens. J. 2008;8:371–381.

[14] Argall BD, Billard AG. A survey of Tactile Human-Robot Interactions. Rob. Auton. Syst. 2010;58:1159–1176.

[15] Göger D, Gorges N, Wörn H. Tactile sensing for an anthropomorphic robotic hand: hardware and signal processing. In: IEEE International Conference on Robotics and Automation. Kobe (Japan); 2009; p. 895–901.

[16] Choi B, Lee S, Choi HR, et al. Development of anthropomorphic robot hand with tactile sensor: SKKU Hand II. In: IEEE International Conference on Intelligent Robots and Systems. Beijing (China); 2006; p. 3779–3784.

[17] Jockusch J, Walter J, Ritter H. A tactile sensor system for a three-fingered robot manipulator. In: 1997 IEEE International Conference on Robotics and Automation. Albuquerque, New Mexico (USA); 1997; p. 3080–3086.

[18] Hosoda K, Tada Y, Asada M. Anthropomorphic robotic soft fingertip with randomly distributed receptors. Rob. Auton. Syst. 2006;54:104–109.

[19] Minato T, Yoshikawa Y, Noda T, et al. CB2: a child robot with biomimetic body for cognitive developmental robotics. In: 2007 7th IEEE-RAS International Conference on Humanoid Robot. HUMANOIDS 2007. Pittsburgh, PA (USA); 2007; p. 557–562.

[20] Saga S, Morooka T, Kajimoto H, et al. High-resolution tactile sensor using the movement of a reflected image. In: Proceedings of Eurohaptics. Paris (France); 2006; p. 81–86.

[21] Yuan W, Li R, Srinivasan MA, et al. Measurement of shear and slip with a GelSight tactile sensor. In: 2015 IEEE International Conference on Robotics and Automation (ICRA). Seattle, WA (USA); 2015; p. 304–311.

[22] Yamada K, Goto K, Nakajima Y, et al. A sensor skin using wire-free tactile sensing elements based on optical connection. In: Proceedings of the 41st SICE Annual Conference. SICE 2002. Osaka (Japan); 2002; p. 131–134.

[23] Yoshikai T, Hayashi M, Ishizaka Y, et al. Development of robots with soft sensor flesh for achieving close interaction behavior. Adv. Artif. Intell. 2012;2012:8–8.

[24] Natale L, Torres-jara E. A sensitive approach to grasping. In: Proceedings of Sixth International Conference on Epigenetic Robotics. Paris (France). Citeseer; 2006; p. 87–94.

[25] Liu T, Inoue Y, Shibata K. Design of low-cost tactile force sensor for 3D force scan. In: Sensors, 2008 IEEE. Lecce (Italy). IEEE; 2008; p. 1513–1516.

[26] Takahashi H, Nakai A, Thanh-Vinh N, et al. A triaxial tactile sensor without crosstalk using pairs of piezoresistive beams with sidewall doping. Sens. Actuators, A. 2013;199:43–48.

[27] Iwata H, Sugano S. Whole-body covering tactile interface for human robot coordination. In: Proceedings. ICRA'02. IEEE International Conference on Robotics and Automation, 2002. Washington, DC (USA); p. 3818–3824.

[28] Cannata G, Maggiali M. An embedded tactile and force sensor for robotic manipulation and grasping. In: 2005 5th IEEE-RAS International Conference on Humanoid Robots. Tsukuba (Japan). IEEE; 2005; p. 80–85.

[29] Bridgwater LB, Ihrke CA, Diftler MA, et al. The Robonaut 2 hand – designed to do work with tools. In: 2012 IEEE International Conference on Robotics and Automation (ICRA). St. Paul, MN (USA); 2012; p. 3425–3430.
[30] Oddo CM, Controzzi M, Beccai L, et al. Roughness encoding for discrimination of surfaces in artificial active-touch. IEEE Trans. Rob. 2011;27:522–533.
[31] Cheng MY, Lin CL, Lai YT, et al. A polymer-based capacitive sensing array for normal and shear force measurement. Sensors. 2010;10:10211–10225.
[32] Lee H, Chung J, Chang S, et al. Normal and shear force measurement using a flexible polymer tactile sensor with embedded multiple capacitors. J. Microelectromech. Syst. 2008;17:934–942.
[33] Hoshi T, Shinoda H. Robot skin based on touch-area-sensitive tactile element. In: 2006 IEEE International Conference on Robotics and Automation, 2006. ICRA 2006. Orlando, FL (USA). IEEE; 2006; p. 3463–3468.
[34] Viry L, Levi A, Totaro M, et al. Flexible three-axial force sensor for soft and highly sensitive artificial touch. Adv. Mater. 2014;26:2659–2664.
[35] Dobrzynska JA, Gijs MAM. Polymer-based flexible capacitive sensor for three-axial force measurements. J. Micromech. Microeng. IOP Publishing. 2013;23:15009 (1–11).
[36] Analog Devices. AD7147: CapTouch® Programmable Controller for Single-Electrode Capacitance Sensors (REV.D). 2011.
[37] Ulmen J, Cutkosky M. A robust, low-cost and low-noise artificial skin for human-friendly robots. In: 2010 IEEE International Conference on Robotics and Automation (ICRA). Anchorage (Alaska): IEEE; 2010; p. 4836–4841.
[38] Davison B. Techniques for Robust Touch Sensing Design. AN1334 Microchip Technol. Inc. Microchip; 2010.
[39] Maggiali M, Cannata G, Maiolino P, et al. Embedded distributed capacitive tactile sensor. In: 11th Mechatronics Forum Biennial International Conference. Limerick (Ireland); 2008.